Systems/Circuits

Neuropilin 2/Plexin-A3 Receptors Regulate the Functional Connectivity and the Excitability in the Layers 4 and 5 of the Cerebral Cortex

Hussain Y. Khdour,[1,3] Krishnakanth Kondabolu,[1] Alina Khadka,[1] Maxime Assous,[1] James M. Tepper,[1] Tracy S. Tran,[2] and Pierre-Olivier Polack[1]

[1]Center for Molecular and Behavioral Neuroscience, Rutgers University–Newark, Newark, New Jersey 07102, [2]Department of Biological Sciences, Rutgers University–Newark, Newark, New Jersey 07102, and [3]Behavioral and Neural Sciences Graduate Program, Rutgers University–Newark, Newark, New Jersey 07102

The functions of cortical networks are progressively established during development by series of events shaping the neuronal connectivity. Synaptic elimination, which consists of removing the supernumerary connections generated during the earlier stages of cortical development, is one of the latest stages in neuronal network maturation. The semaphorin 3F coreceptors neuropilin 2 (Nrp2) and plexin-A3 (PlxnA3) may play an important role in the functional maturation of the cerebral cortex by regulating the excess dendritic spines on cortical excitatory neurons. Yet, the identity of the connections eliminated under the control of Nrp2/PlxnA3 signaling is debated, and the importance of this synaptic refinement for cortical functions remains poorly understood. Here, we show that Nrp2/PlxnA3 controls the spine densities in layer 4 (L4) and on the apical dendrite of L5 neurons of the sensory and motor cortices. Using a combination of neuroanatomical, *ex vivo* electrophysiology, and *in vivo* functional imaging techniques in *Nrp2* and *PlxnA3* KO mice of both sexes, we disprove the hypothesis that Nrp2/PlxnA3 signaling is required to maintain the ectopic thalamocortical connections observed during embryonic development. We also show that the absence of Nrp2/PlxnA3 signaling leads to the hyperexcitability and excessive synchronization of the neuronal activity in L5 and L4 neuronal networks, suggesting that this system could participate in the refinement of the recurrent corticocortical connectivity in those layers. Altogether, our results argue for a role of semaphorin–Nrp2/PlxnA3 signaling in the proper maturation and functional connectivity of the cerebral cortex, likely by controlling the refinement of recurrent corticocortical connections.

Key words: cortex maturation; cortical layers; functional connectivity; sema 3F signaling; synaptic pruning; thalamocortical

Significance Statement

The function of a neuronal circuit is mainly determined by the connections that neurons establish with one another during development. Understanding the mechanisms underlying the establishment of the functional connectivity is fundamental to comprehend how network functions are implemented, and to design treatments aiming at restoring damaged neuronal circuits. Here, we show that the cell surface receptors for the family of semaphorin guidance cues neuropilin 2 (Nrp2) and plexin-A3 (PlxnA3) play an important role in shaping the functional connectivity of the cerebral cortex likely by trimming the recurrent connections in layers 4 and 5. By removing the supernumerary inputs generated during early development, Nrp2/PlxnA3 signaling reduces the neuronal excitability and participates in the maturation of the cortical network functions.

Received Sep. 28, 2021; revised Mar. 8, 2022; accepted Mar. 15, 2022.

Author contributions: H.Y.K., K.K., T.S.T., and P.-O.P. designed research; H.Y.K., K.K., A.K., and M.A. performed research; J.M.T. contributed unpublished reagents/analytic tools; H.Y.K., K.K., A.K., and P.-O.P. analyzed data; H.K. and P.-O.P. wrote the paper; T.S.T. edited the paper.

This work was funded by the Rutgers-Newark Chancellor's Seed Grant Program (to P.-O.P. and T.S.T), National Institutes of Health (NIH)/National Eye Institute Grant R01-EY-030860 (to P.-O.P), NIH/National Institute of Neurological Disorders and Stroke Grant R05-NS-034865 and R01-NS-034865 (to J.M.T.), New Jersey Governor's Council for Medical Research and Treatment of Autism Grant CAUT17BSP022 (to T.S.T.), National Science Foundation/Integrative Organismal Systems Grants 1556968 and 2034864 (to T.S.T.) and Brain and Behavior Research Foundation (NARSAD Young Investigator) and Rutgers Busch Biomedical Grant (to M.A.). We thank Edward Martinez for advice on Golgi staining, as well as Candice Chavez and Drew Headley for guidance for the retrograde tracing experiments.

The authors declare no competing financial interests.

Correspondence should be addressed to Pierre-Olivier Polack at polack.po@rutgers.edu or Tracy S. Tran at tstran@rutgers.edu.

https://doi.org/10.1523/JNEUROSCI.1965-21.2022

Introduction

The functional connectivity of the adult nervous system results from an orderly series of events: neuronal migration, axon guidance and dendrite growth during embryonic development, followed by synaptogenesis, axonal and dendritic pruning, and synaptic plasticity during postnatal stages (Stiles and Jernigan, 2010). These processes are orchestrated by several guidance protein families (Tessier-Lavigne and Goodman, 1996), including the semaphorins, a family of secreted and membrane-associated attractants and repellants (Tran et al., 2007; Pasterkamp, 2012). Converging evidence suggests that the secreted ligand semaphorin 3F (Sema3F) plays an important role in the establishment of the cortical connectivity when binding its holoreceptor

complex formed by neuropilin (Nrp2) and plexin-A3 (PlxnA3; Giger et al., 2000; Bagri et al., 2003; Hota and Buck, 2012; Kong et al., 2016) by enabling the elimination of the excess number of dendritic spines generated during development (Tran et al., 2009; Demyanenko et al., 2014). Indeed, cortical neurons are heavily connected to each other at birth, but most of those connections are progressively eliminated during childhood and adolescence (Holtmaat et al., 2006; Alvarez et al., 2007). This synapse elimination is concomitant with the functional maturation of the cortex (Hoy and Niell, 2015). When Sema3F–Nrp2/PlxnA3 signaling is absent during development, layer 5 (L5) pyramidal neurons in the primary somatosensory cortex (S1) of *Sema3F*$^{-/-}$ and *Nrp2*$^{-/-}$ display supernumerary spines after postnatal day 14 (P14), but only on the section of the primary apical dendrite immediately proximal to the soma (Tran et al., 2009). This dendritic compartment of L5 neurons, which is mainly located within the thalamocortical (TC) recipient L4, contains very little spines in wild type (WT). The role of Sema3F seems restricted to the L4 region as supernumerary spines were also found in the L4 of the primary visual cortex (V1) of *Sema3F*$^{-/-}$ mice at P21 (Demyanenko et al., 2014). Moreover, no abnormalities in spine density were reported in the S1 L2/3 from *Nrp2*$^{-/-}$ mutants (Tran et al., 2009). Another finding suggests that Sema3F–Nrp2 signaling is involved in the establishment of the thalamocortical connectivity. During early cortical development, Sema3F is expressed following a posteroanterior gradient (Demyanenko et al., 2011) and the absence of Sema3F–Nrp2 signaling results at P7 in thalamic axons of nonvisual relay nuclei projecting into V1 (Demyanenko et al., 2011). However, it is not known whether those aberrant thalamocortical connections are still present in the adult. Moreover, we do not know whether the dendritic spine refinement by Sema3F is similar across cortices as the presence of supernumerary spines in L4 was only demonstrated in the V1 of *Sema3F*$^{-/-}$ mice (Demyanenko et al., 2014), and spine counting in L5 and L2/3 neurons was only performed in the S1 of *Sema3F*$^{-/-}$ and *Nrp2*$^{-/-}$ mice (Tran et al., 2009). We also needed to further assess the impact of those supernumerary spines on cortical excitability as previous studies reported an increase in miniature excitatory postsynaptic current frequency in the S1 of *Nrp2*$^{-/-}$ mice (Tran et al., 2009) as well as a greater propensity of developing epileptic seizures (Sahay et al., 2005; Eisenberg et al., 2021).

Hence, we performed a systematic survey of the spine density in L4, L2/3, and L5 of V1, S1, and primary motor cortex (M1) to determine the dendritic spine phenotypes resulting from the absence of Nrp2/PlxnA3 signaling across layers and across cortices. Using retrograde tracing, we demonstrated that the mistargeting of V1 by nonvisual thalamocortical axons at P7 is resolved in adult animals. Then, we combined optogenetic and *ex vivo* whole-cell recordings to test the hypothesis that PlxnA3 signaling is required for establishing the proper functional connectivity between the lateral geniculate nucleus (LGN) and L4 and L5 neurons. We further assessed the functional connectivity in the different layers of the visual cortex by performing *in vivo* calcium imaging in WT mice and Nrp2/PlxnA3 knock-out (KO) mice. Altogether, our results rebut the hypothesis of a role for Nrp2/PlxnA3 signaling in the maturation of the thalamocortical connectivity and provide evidence of its importance for the maturation of the cortical functional connectivity.

Materials and Methods

All the procedures described below were approved by the Institutional Animal Care and Use Committee of Rutgers University. We used male and female adult mice. KO mice were either *PlxnA3*$^{-/-}$ or *Nrp2*$^{-/-}$. All mutant mouse lines used in this study have been backcrossed for at least 10 generations to the C57BL/6NTac background stain. WT mice (*PlxnA3*$^{+/-}$ or *Nrp2*$^{+/-}$) were the littermates of KO mice.

Golgi staining. Mice were anesthetized with 5% isoflurane then killed by cervical dislocation. Brains were harvested and incubated in Golgi solution A + B (FD Rapid Golgi Stain Kit, FD NeuroTechnologies) for 7 d. After incubation, brains were washed with Solution C for 8 h at room temperature, then embedded in O.C.T. Compound embedding medium (Tissue-Tek). Coronal sections (100 μm) from V1, S1, and M1 were sectioned by a cryostat and mounted on 3% gelatin-coated slides for staining with solution D + E, as previously published (Tran et al., 2009). Following increasing concentration of ethanol dehydration (50−100%), the brain sections were cleared with xylene and coverslips were placed in Permount. All slides were dried in the dark at room temperature for at least 24 h before photodocumentation with microscopy.

Quantification of spine density. Golgi-stained neurons were imaged using a bright-field microscope (AxioExaminer Z1, Zeiss). Compiled *z*-stack images were exported in ImageJ for measurement and contrast adjustment. Spine densities were scored in 20 μm segments of the proximal and distal parts of the apical dendrite of L5 and L2/3 neurons as well as basal dendrites and secondary dendritic branches of L4 neurons.

Retrograde tracing. Mice were anesthetized with isoflurane and placed in a stereotaxic frame. A small craniotomy was performed above the left V1 [anteroposterior (AP), −0.5 mm (λ); mediolateral (ML), 2.1 mm]. The retrograde tracer FastBlue (Polysciences; 90 nl) was injected at the border between L4 and L5 (depth, 450 µm) using a Nanoliter Injector (WPI). After injection, the skin was sutured and the mouse was released in its cage. Seven days later, mice were anesthetized and perfused by intracardiac injection of paraformaldehyde. Brains were placed in 30% sucrose solution for a few days and then imbedded in O.C.T. Compound. The entire brain was sliced in 50-μm-thick coronal sections. All sections were imaged using a confocal microscope.

Retrograde tracing analysis. Cortical and subcortical structures were identified and mapped using the Franklin and Paxinos (2013) mouse brain atlas. Neurons labeled by FastBlue were located independently by another experimenter blind to the mouse phenotype. Maps and the labeled neuron positions were merged to identify cortical and subcortical structures targeting V1. The size and location of the injection site were inspected to ensure that only V1 was affected by the injection. We took two sections from each anterior, middle, and posterior parts of the thalamus, quantified all the cells labeled by FastBlue in each thalamic nucleus, then, for each animal, we divided the number of cells of each nucleus by the total number of cells labeled in the thalamus.

Channelrhodopsin-2 injection. Mice were anesthetized with isoflurane (1–3% v/v mixed with oxygen). Body temperature was maintained at 37°C using a homeothermic heating pad. The surgical site was disinfected with alcohol and betadine. The skin was incised above the V1 (2.5 mm posterior and 2.5 mm lateral from bregma), and a small craniotomy was performed. The LGN was injected with 100 µl of AAV5-CAMKIIa-hChR2(H134R)-EYFP vector using a glass pipette (depth, 2.6 mm). The virus was injected at a rate of 20 nl/min. The glass pipette was left in place for ~10 min to minimize virus backflow. Analgesia was maintained postsurgery with carprofen (5 mg/kg). We waited between 42 and 56 d after the injection to allow for expression of the channelrhodopsin-2 (ChR2) protein. Mice were then anesthetized and perfused for *ex vivo* slice recordings and anatomic verification of ChR2 expression.

Ex vivo *slice recordings.* Infrared (IR) differential interference contrast imaging was used for whole-cell patch-clamp recordings in slices acutely prepared from KO and WT mice. Briefly, mice were anesthetized with isoflurane, followed by an injection of ketamine/xylazine (respectively, 80/20 mg/kg, i.p.; Henry Schein). Mice were then transcardially perfused with ice-cold oxygenated *N*-methyl-D-glucamine (NMDG)-based solution that contained the following (in mM): 103.0 NMDG, 2.5 KCl, 1.2 NaH_2PO_4, 30.0 NaHCO3, 20.0 HEPES, 25.0 dextrose, 101.0 HCl, 10.0 $MgSO_4$, 2.0 Thiourea, 3.0 sodium pyruvate, 12.0 *N*-acetyl cysteine, and 0.5 CaCl2, saturated with 95% O_2 and 5% CO_2; 300–310 mOsm and pH 7.2–7.4. The brain was quickly removed from the skull and blocked in a coronal or parasagittal plane then glued to the stage of

a vibrating microtome (model VT1200S, Leica Microsystems). The brain was subsequently submerged in oxygenated ice-cold NMDG-based solution that was maintained at −4°C. Brain slices having a thickness of 300 μM were then cut and transferred to a holding chamber containing oxygenated NMDG-based solution at 35°C for 5 min. Then, brain slices were transferred to a chamber containing oxygenated artificial CSF (ACSF) at 25°C until used. The ACSF contained the following (in mM): 124 NaCl, 26 NaHCO3, 2.5 KCl, 1.2 NaH_2PO_4, 1 MgCl2, 2 CaCl2, 10 glucose, and 3 sodium pyruvate. The osmolarity and pH of the ACSF were 300–310 mOsm and 7.2–7.4, respectively. The recording chamber was perfused continuously (2–3 ml/min) with oxygenated ACSF maintained at 32–34°C. Slices at the level of virus injections were collected and kept in a fixative solution [4% w/v paraformaldehyde (PFA) in PBS for 1–2 d at 4°C] for *post hoc* anatomic verification of ChR2 expression in the LGN.

The whole-cell slice recording setup consisted of a microscope (model BX50WI, Olympus) equipped with a 40× water-immersion objective lens (LUMPIanFL/IR, Olympus) for visualizing brain slices. The microscope had an iXon EMCCD (electron-multiplying CCD) camera (model DU-885K-CS0, Andor), with a halogen light source (TH3 power supply, Olympus), and imaging software (Solis version 4.4.0, Andor). A mercury lamp (model BH2-RFL-T3 power supply, Olympus) coupled to appropriate filter cubes (model U-M41001, Olympus; model 49008, Chroma Technology) was used to visualize the fluorescence of LGN terminal field in layer 4 of visual cortex. Somatic patch-clamp recordings of pyramidal neurons were made in a whole-cell configuration (in voltage-clamp mode at a holding voltage (V_h) of −70 mV, and/or in current-clamp mode) using glass pipettes that were filled with a K-gluconate-based solution composed of the following (in mM): 130 K-gluconate, 10 KCl, 2 MgCl2, 10 HEPES, 4 Na2ATP, and 0.4 Na3GTP, with osmolarity of 290–295 mOSm, and pH 7.3. The internal solution also contained either a 0.2% w/v biocytin (catalog B4261, Sigma-Aldrich) or 1.5 μl/ml Alexa Fluor 594 dye (catalog #A10438, Thermo Fisher Scientific) to facilitate their *post hoc* anatomic identification and localization.

The recording pipettes typically had an impedance of 3–5 MΩ. Patch-clamp recordings were obtained using a Multiclamp 700B amplifier (Molecular Devices) and ITC-1600 digitizer (Instrutech), with AxoGraph software (version 1.7.4) used for data acquisition and analysis. Electrode signals were low-pass filtered (Bessel filter) at 1 or 10 kHz for voltage-clamp or current-clamp recordings, respectively, and sampled at 20 kHz.

Postsynaptic responses were evaluated by using NMDA and AMPA receptor receptor antagonists (AP-5 and CNQX, respectively, 10 μM). We used tetrodotoxin (TTX; 1 μM) in conjunction with 4-aminopyridine (4-AP; 1 mM) to determine the monosynaptic nature of the synaptic responses (Yamawaki et al., 2016).

Optogenetic stimulation of ChR2-expressing axons was performed by a transistor–transistor logic-controlled LED (catalog #LB W5SN-GZJX-35-Z, Mouser Electronics; pulse duration, 2 ms; pulse wavelength, 470 nm) that was placed below the slice chamber. EPSPs or EPSCs were assessed from the average amplitude of at least 10 trials. Response latencies were calculated as the time difference from the onset of optogenetic stimulation to the onset of the postsynaptic response.

Immunohistochemistry. Brain slices that had whole-cell patched neurons were placed in a fixative solution (4% PFA, 15% picric acid) for 1–2 d. Slices were then washed with PBS Triton (0.3%). Pyramidal neurons that were filled with biocytin were then incubated overnight with Alexa Fluor 405-conjugated streptavidin (1:500 dilution; catalog #S32351, Thermo Fisher Scientific) or Alexa Fluor 594-conjugated streptavidin (catalog #S32356, Thermo Fisher Scientific) at a similar 1:500 dilution. Slices were then washed in PBS and mounted on a glass slide, coverslipped in Vectashield Mounting Medium, and imaged on a confocal microscope (model FluoView FV1000, Olympus).

Head bar implants for calcium imaging. Ten minutes after systemic injection of an analgesic (carprofen, 5 mg/kg body weight), adult (age, 3–6 months) mice were anesthetized with isoflurane (5% induction, 1.2% maintenance) and placed in a stereotaxic frame. Body temperature was kept at 37°C using a feedback-controlled heating pad. Pressure points and incision sites were injected with lidocaine (2%). Eyes were protected from desiccation with artificial tear ointment (Dechra). Next, the skin covering the skull was incised and a custom-made lightweight metal head bar was glued to the skull using Vetbond (3M). In addition, a large recording chamber capable of retaining the water necessary for using a water-immersion objective was built using dental cement (Ortho-Jet, Lang). Mice recovered from surgery for 5 d, during which amoxicillin was administered in drinking water (0.25 mg/ml).

AAV virus injection for in vivo *calcium imaging.* After recovery, mice were anesthetized using isoflurane as described above. A circular craniotomy (diameter = 3 mm) was performed above V1. The adeno-associated virus (AAV) vector AAV1.eSyn.GCaMP6f.WPRE.SV40 (UPenn Vector Core) carrying the gene of the fluorescent calcium sensor GCaMP6f was injected at three sites 500 μm apart around the center of V1 (stereotaxic coordinates, distance from bregma: AP, −4.0 mm; ML, +2.2 mm) using a MicroSyringe Pump Controller Micro 4 (WPI) at a rate of 30 nl/min. Injections started at a depth of 550 μm below the pial surface, and the tip of the pipette was raised in steps of 100 μm during the injection, up to a depth of 200 μm below the dura surface. The total volume injected across all depths was 0.7 μl. After removal of the injection pipette, a 3-mm-diameter coverslip was placed over the dura, such that the coverslip fits entirely in the craniotomy and was flush with the skull surface. The coverslip was kept in place using Vetbond and dental cement. Mice were left to recover from the surgery for at least 3 weeks to obtain a satisfactory gene expression.

In vivo *functional imaging.* During the last week of recovery, mice were trained to stay on a spherical treadmill consisting of a ball floating on a small cushion of air that allowed for full 2D movement (McClure and Polack, 2019). During three daily 20 min sessions, the mouse head bar was fixed to a post holding the mouse on the apex of the spherical treadmill. Functional imaging was performed at 15 frames/s using a resonant scanning two-photon microscope (Neurolabware) powered by a Ti-Sapphire Ultra-2 laser (Coherent) set at 910 nm. The laser beam was focused 200 μm below the cortical surface using a 16×, 0.8 numerical aperture Nikon water-immersion objective. The objective was tilted 30° such that the objective lens was parallel to the dura surface. Laser power was kept at <70 mW. Frames (512 × 796 pixels) were acquired using the software Scanbox developed by Neurolabware.

Visual stimuli. A gamma-corrected 40 cm diagonal LCD monitor was placed 30 cm from the eye contralateral to the craniotomy such that it covered the entire monocular visual field. Visual stimuli were generated in MATLAB (MathWorks) using the Psychtoolbox (Brainard, 1997). They consisted of the presentation of a series of drifting sine-wave gratings (12 orientations evenly spaced by 30° and randomly permuted) with the following parameters: temporal frequency, 2 Hz; spatial frequency, 0.04 cycle/°; contrast, 75%; duration, 1.5 s; intertrial interval, 3 s). A photodiode located at the top left corner of the screen was used to detect the exact timing of the visual stimuli onset and offset.

Calcium imaging analysis. All the analyses detailed below were performed using custom MATLAB routines. Calcium imaging frames were realigned offline to remove movement artifacts using the Scanbox algorithm (Neurolabware). A region of interest (ROI) was determined for each neuron using a semiautomatic segmentation routine. For every frame, the fluorescence level was averaged across the pixels of the ROI. Potential contamination of the soma fluorescence by the local neuropil was removed by subtracting the mean fluorescence of a 2–5 μm ring surrounding the ROI of the neuron, excluding the soma of neighboring neurons, and then adding the median value across time of the subtracted background. We then computed the fractional fluorescence from the background subtracted fluorescence data. The fractional fluorescence [$dF/F = (F - F_0)/F_0$], was calculated with F_0 defined as the median of the raw fluorescence measured during every intertrial interval. Trials were then sorted by stimulus. The mean dF/F measured during a 1.5 s intertrial period immediately preceding each visual stimulation was subtracted from the dF/F measured during the trial.

Orientation tuning. For each trial, we computed the summed baseline-subtracted dF/F measured during the 1.5 s presentation of the 12 different drifting gratings used to construct the tuning curve. Using a resampling-based Bayesian method on the summed dF/F of individual trials (Cronin et al., 2010), we estimated the best orientation tuning curve of four models (constant, circular Gaussian 180, circular Gaussian 360, and direction-selective circular Gaussian). The preferred (pref.) orientation of the neuron was defined as the orientation for which the value of the estimated tuning curve was at its maximum.

Correlation analysis. For each imaging session, the fractional fluorescence of each neuron recorded during the whole imaging session was correlated successively with the fractional fluorescence of each other neuron of the recording using the xcorr MATLAB function. The instantaneous correlation ($t = 0$ ms) of each pair was averaged with the instantaneous correlation of pairs having the same distance between their preferred orientations (bin size, 1°).

Statistical analysis. For each mouse, we computed for each dendritic tree locations the median spine density across all the neurons located in a same layer and a same cortical area. We then tested the effects of the genotype (WT or KO), genetic background (Nrp2 or PlxnA3), cortical areas (V1, S1, or M1), and dendritic tree locations using a four-way ANOVA (anovan function in MATLAB). The Tukey's HSD was used for multiple comparisons. Using neurons instead of animals as a biological replicate led to the same results and the same conclusions. Statistical tests were performed using MATLAB version 2019b.

Results

Cortical dendritic spine defects in the absence of Nrp2/PlxnA3 signaling

To better understand the exact role of Sema3F–Nrp2/PlxnA3 signaling in the maturation of the cortical networks, it was necessary to extend and unify the analyses made by previous studies (Tran et al., 2009; Demyanenko et al., 2011, 2014) whereby the experiments performed and the data collected were not from the same layers, the same cortices, and the same mutants. Thus, we needed to determine the exact distribution of the abnormal dendritic spine densities in the different cortical layers, whether Nrp2/PlxnA3 signaling has the same role in the different sensory and motor cortices, and verify that the deletion of *PlxnA3* or *Nrp2* leads to the similar synaptic density phenotype. Hence, we started by examining the spine density of the primary and secondary branches of neurons located in V1 L4 (Fig. 1*A*) of mice with deletion in the gene for *PlxnA3* KO mice (mean ± SD age, 4.7 ± 1.2 months; age range, 4–6 months) or $PlxnA3^{-/-}$ and their littermate controls (*PlxnA3* WT or *PlxnA3* heterozygote: $PlxnA3^{+/+}$ or $PlxnA3^{+/-}$, respectively; age, 4.7 ± 1.2 months; age range, 4–6 months). We also counted the number of spines located on the basal dendrites, and on the proximal and mid-section of the primary apical dendrite of neurons located in V1 L2/3 and V1 L5 of *PlxnA3* KO and *PlxnA3* WT mice (Fig. 1*B*,*C*, respectively). We then compared the spine densities layer by layer in V1 between *PlxnA3* KO and *PlxnA3* WT mice (Fig. 1*D*–*F*). We found a significant increase in the density of spines located on the primary and secondary dendritic branches of L4 neurons in the absence of the *PlxnA3* receptor (Fig. 1*D*; $F = 50.00$, $p < 0.001$), supporting earlier findings in the V1 of $Sema3F^{-/-}$ mice (Demyanenko et al., 2014). Then, we compared the spine density of the V1 L2/3 neurons (Fig. 1*E*) of *PlxnA3* KO and *PlxnA3* WT mice and performed a similar comparison in V1 L5 (Fig. 1*F*). The spine density found in the different dendritic sections of V1 L2/3 were similar between WT and KO ($F = 1.65$, $p = 0.22$). However, we found a significant increase in the density of spine on the proximal section and mid-section of the primary apical dendrite of V1 L5 neurons in *PlxnA3* KO mice compared with WT mice ($F = 33.49$, $p < 0.001$), a finding similar to what had been previously shown in the S1 of *Nrp2* KO mice, the ligand-binding receptor of Sema3F (Tran et al., 2009). To determine whether the layer distribution of the spine density abnormalities depended on Nrp2, we performed the same experiment in *Nrp2* KO mice ($Nrp2^{-/-}$; age, 4.4 ± 1.4 months; age range, 3–6 months) and *Nrp2* WT mice ($Nrp2^{+/+}$; age, 4.5 ± 0.9 months; age range, 3–6 months). We found the same supernumerary spine phenotype in *Nrp2* KO mice as that seen in *PlxnA3* mice, on the primary and secondary dendrites of L4 and on the proximal section and mid-section of the apical dendrite of L5 neurons, while no abnormal spine densities were observed on L2/3 neurons or on the basal dendrites of L5 neurons in either one of the mutant animals (Fig. 1*G*–*I*: L4: $F = 72.81$, $p < 0.001$; $F = 0.44$, $p = 0.46$; L5: $F = 435.09$, $p < 0.001$).

Since during development Sema3F is expressed in a posteroanterior gradient (Demyanenko et al., 2011; Shiflett et al., 2017), we hypothesized that the spine phenotype found in more anterior cortices such as S1 or the M1 could differ from the one we found in V1. Therefore, we measured the spine densities on the different dendritic sections of L4 (primary or secondary branches), L2/3, and L5 neurons (basal dendrite, proximal, and mid-section of the apical dendrite) located in S1 and M1 of mice KO for *PlxnA3* or *Nrp2* (three and five mice, respectively) and their WT littermates (three and four mice, respectively). We used a four-way ANOVA to determine the influence of the genotype (WT or KO), the dendritic section, the genetic background (*PlxnA3* or *Nrp2*), and the cortex location on the spine density phenotype. We found significant differences between genotypes (WT or KO) in L4 (genotypes: $F = 226.95$, $p < 0.001$) and L5 (genotypes: $F = 456.41$, $p < 0.001$). However, spine densities in L2/3 did not present significant differences between genotypes (genotypes: $F = 0.03$, $p = 0.87$). We then performed pairwise Tukey's HSD *post hoc* comparisons and organized the results in bee swarm plots that reported the spine density in the different layers of the different genotypes (WT or KO), backgrounds (*PlxnA3* and *Nrp2*), as well as the statistical significance of the pairwise *post hoc* comparisons in V1 (Fig. 1*D*–*I*), S1 (Fig. 2*A*–*F*), and M1 (Fig. 2*G*–*J*). For L4 neurons, we found significantly higher spine densities in KO than in WT mice in primary and secondary branches of V1 (Fig. 1*A*,*D*,*G*) and S1 (Fig. 2*A*,*D*) neurons for both *PlxnA3* and *Nrp2* genetic backgrounds (Tukey's HSD *post hoc* test: *PlxnA3* V1 L4 primary branches, $p = 0.013$; *PlxnA3* S1 L4 primary branches, $p = 0.015$; *PlxnA3* V1 L4 secondary branches, $p = 0.007$; *PlxnA3* S1 L4 secondary branches, $p = 0.008$; *Nrp2* L4 all areas and branches, $p < 0.001$). In L2/3, we did not find significant differences between KO and WT phenotypes in any cortices (V1: Fig. 1*B*,*E*,*H*; S1: Fig. 2*B*,*E*; M1: Fig. 2*G*,*I*; Tukey's HSD *post hoc* test, $p > 0.05$ for the three dendritic branch location). However, the L5 neurons of KO mice presented more spines on the proximal and mid-section of their apical dendrites than in WT in both *Nrp2* and *PlxnA3* mice (V1: Fig. 1*C*,*F*,*I*; S1: Fig. 2*C*,*F*; M1: Fig. 2*H*,*J*; Tukey's HSD *post hoc* test, $p < 0.001$ for both branches), but the density of spine located in L5 basal dendrites was similar between WT and KO mice (Tukey's HSD *post hoc* test, $p > 0.05$). Altogether, our spine density survey showed that the role of Nrp2/PlxnA3 signaling is similar across cortices and across mutants with stereotypical spine elimination defects in the primary and secondary branches of L4 neurons and in the proximal and mid-section of the apical dendrite of L5 neurons. However, the density of supernumerary spines in L4 and L5 cortical neurons was greater when the KO mutation affected the coreceptor *Nrp2* than when the mutation

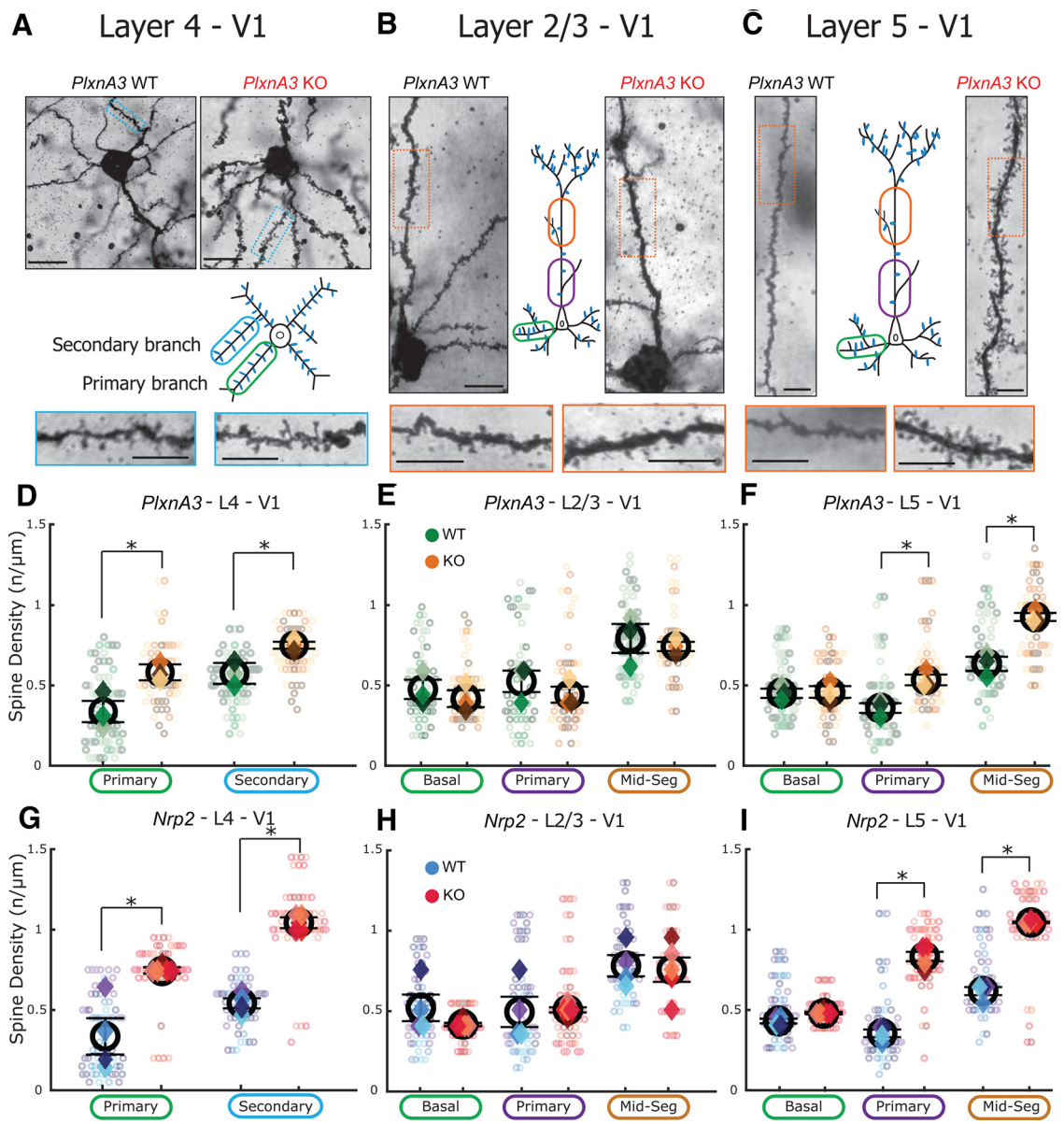

Figure 1. Comparison of the spine density of L4, L2/3, and L5 V1 neurons in the presence and absence of Nrp2/PlxnA3 signaling. ***A***, Photomicrographs of an L4 spiny stellate neuron taken in a mouse that does not express the Sema3F coreceptor PlexinA3 (right; *PlxnA3* KO) and a wild-type littermate (left; *PlxnA3* WT). Scale bar, 15 µm. Inset, Schematic representation of the location of the primary and secondary branches on an L4 neurons. Bottom, Enlargements of the sections indicated in the above photomicrographs. Scale bar, 10 µm. ***B***, Same representation as in ***A*** for V1 L2/3 pyramidal cells. ***C***, Same representation as in ***A***, for V1 L5 pyramidal cells. ***D***, Spine density in the primary and secondary branches of V1 L4 neurons in *PlxnA3* WT (neurons, green dots; median across neurons for each mouse, green diamonds) and *PlxnA3* KO (neurons, brown dots; median across neurons for each mouse, brown diamonds). *PlxnA3* WT, 65 neurons in 3 mice; *PlxnA3* KO, 60 neurons in 3 mice (Fig. 2*K*, color code). Black circles indicate the mean across mice ± SEM. ***E***, Same representation as in ***D*** for V1 L2/3 pyramidal neurons. *PlxnA3* WT, 60 neurons in 3 mice; *PlxnA3* KO, 57 neurons in 3 mice. ***F***, Same representation as in ***D*** for V1 L5 pyramidal neurons. *PlxnA3* WT, 62 neurons in 3 mice; *PlxnA3* KO, 64 neurons in 3 mice. ***G***, Comparison between *Nrp2* WT (neurons, blue dots; median across neurons for each mouse, blue diamonds) and *Nrp2* 2 KO (neurons, red dots; median across neurons for each mouse, red diamonds) of the spine density in the primary and secondary branches of V1 L4 neurons. *Nrp2* WT, 64 neurons in 4 mice; *Nrp2* KO, 72 neurons in 5 mice (Fig. 2*K*, color code). ***H***, Same representation as in ***G*** for V1 L2/3 pyramidal neurons. *Nrp2* WT, 62 neurons in 4 mice; *Nrp2* KO, 64 neurons in 5 mice. ***I***, Same representation as in ***G*** for V1 L5 pyramidal neurons. *Nrp2* WT, 62 neurons in 4 mice; *Nrp2* KO, 67 neurons in 5 mice. Proximal, Proximal section of the apical dendrite; Mid-Seg, midsegment of the apical dendrite.

targeted *PlxnA3* [four-way ANOVA, influence of genetic background (*PlxnA3* or *Nrp2*): L4: $F = 26.88$, $p < 0.001$; L5: $F = 57.59$, $p < 0.001$; L2/3: $F = 0.46$, $p = 0.49$].

Thalamocortical wiring

The main goal of our investigation was to determine the nature of the connections controlled by Nrp2/PlxnA3 signaling. One possible origin for those supernumerary spines found in L4 neuron primary and secondary branches and in the proximal and mid-section of the apical dendrite of L5 neurons is that they are the result of ectopic thalamocortical connections. Indeed, anterograde tracing experiments had shown that at P7, motor and somatosensory thalamic axons send aberrant projections to V1 in $Nrp2^{-/-}$ mice (Demyanenko et al., 2011). However, it is not known whether those connections are still present in the adult cortex. For other semaphorin signaling systems, similar initial misguidance occurring during early development was shown to be corrected in the adult (Little et al., 2009). To test this hypothesis, we injected the retrograde tracer Fast Blue in V1 of adult mice (*PlxnA3* WT mice, 4.3 ± 1.2 months; *PlxnA3* KO mice,

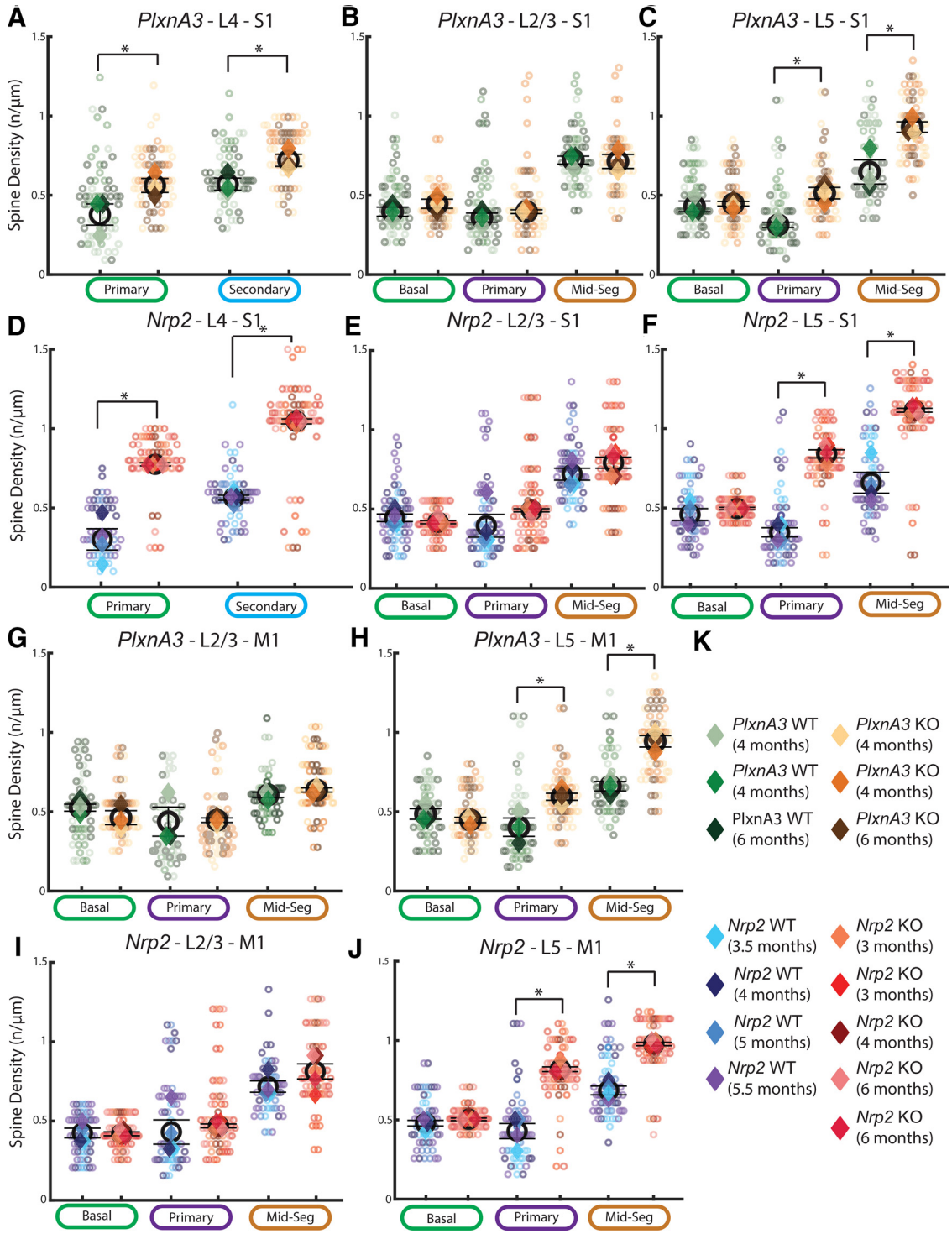

Figure 2. Spine density across layers, cortices, genetic backgrounds, dendritic locations, and genotypes. ***A***, Spine density in the primary and secondary branches of S1 L4 neurons in *PlxnA3* WT (neurons, green dots; median across neurons for each mouse, green diamonds) and *PlxnA3* KO (neurons, brown dots; median across neurons for each mouse, brown diamonds). *PlxnA3* WT, 64 neurons in 3 mice; *PlxnA3* KO, 64 neurons in 3 mice (see color code in ***K***). ***B***, Same representation as in ***A*** for S1 L2/3 pyramidal neurons. *PlxnA3* WT, 62 neurons in 3 mice; *PlxnA3* KO, 58 neurons in 3 mice. ***C***, Same representation as in ***D*** for S1 L5 pyramidal neurons. *PlxnA3* WT, 63 neurons in 3 mice; *PlxnA3* KO, 64 neurons in 3 mice. ***D***, Comparison between *Nrp2* WT (blue) and *Nrp2* KO (neurons, red dots; median across neurons for each mouse, red diamonds) of the spine density in the primary and secondary branches of S1 L4 neurons. *Nrp2* WT, 64 neurons in 4 mice; *Nrp2* KO, 72 neurons in 5 mice. ***E***, Same representation as in ***D*** for S1 L2/3 pyramidal neurons. *Nrp2* WT, 62 neurons in 4 mice; *Nrp2* KO, 70 neurons in 5 mice. ***F***, Same representation as in ***D*** for S1 L5 pyramidal neurons. *Nrp2* WT, 64 neurons in 4 mice; *Nrp2* KO, 72 neurons in 5 mice. ***G***, Spine density in the basal, primary, and midsegment branches of M1 L2/3 neurons in WT (neurons, green dots; median across neurons for each mouse, green diamonds) and *PlxnA3* KO (neurons, brown dots; median across neurons for each mouse, brown diamonds). *PlxnA3* WT, 56 neurons in 3 mice; *PlxnA3* KO, 65 neurons in 3 mice. ***H***, Same representation as in ***G*** for M1 L5 pyramidal neurons. *PlxnA3* WT, 58 neurons in 3 mice; *PlxnA3* KO, 61 neurons in 3 mice. ***I***, Comparison between *Nrp2* WT (neurons, blue dots; median across neurons for each mouse, blue diamonds) and *Nrp2* 2 KO (neurons, red dots; median across neurons for each mouse, red diamonds) of the spine density in the basal, primary, and midsegment branches of M1 L2/3 neurons. *Nrp2* WT, 64 neurons in 4 mice; *Nrp2* KO, 72 neurons in 5 mice. ***J***, Same representation as in ***I*** for M1 L5 pyramidal neurons. *Nrp2* WT, 58 neurons in 4 mice; *Nrp2* KO, 73 neurons in 5 mice. ***K***, Color code attributed to the *PlxnA3* mice (WT, green shades; KO, brown shades) and *Nrp2* mice (WT, blue shades; KO, red shades) and their corresponding age.

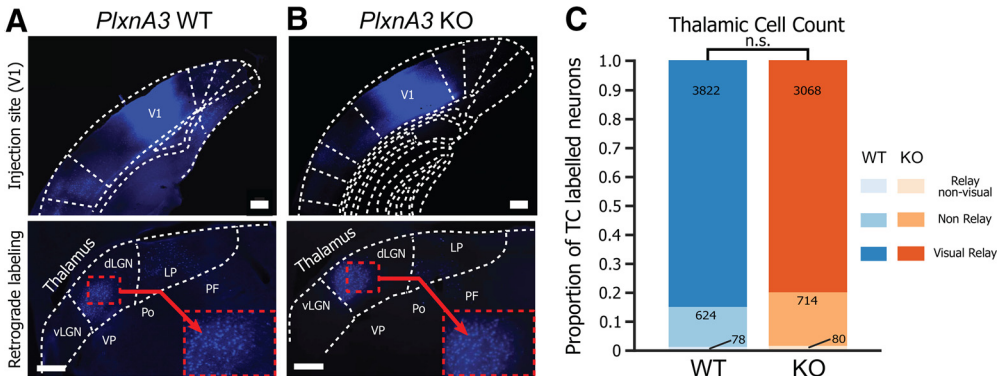

Figure 3. fast blue retrograde labeling from V1 in the thalamic nuclei of adult *PlxnA3* WT and *PlxnA3* KO mice. ***A***, Confocal images of the injection site localized in V1 and the neurons retrogradely labeled in the posterior thalamic nuclei in an adult WT littermate of *PlxnA3* KO mice. vLGN, Ventral part of the LGN; dLGN, dorsal part of the LGN; LP, lateral posterior nucleus; VP, ventral posterior nucleus; Po, posterior thalamic nucleus; PF, parafascicular thalamic nucleus. Scale bar, 100 µm. ***B***, Same representation as in ***A*** for fast blue retrograde labeling performed in an adult *PlxnA3* KO mouse. ***C***, Proportion of neurons labeled in the visual relay, relay nonvisual, and nonrelay thalamic nuclei for WT mice and mice KO for PlxnA3 the coreceptor of Sema3F. χ^2 test: $\chi^2 = 0.11$; n.s., nonsignificant difference ($p = 0.74$).

4.3 ± 1.2 months) and compared the location of the neurons retrogradely labeled in the thalamus between *PlxnA3* WT mice (Fig. 3*A*) and *PlxnA3* KO mice (Fig. 3*B*). We did not find any difference in the origin of thalamic neurons projecting to V1 between KO and WT mice (Fig. 3*C*; χ^2 tests, $p > 0.1$; three WT mice, three KO mice). Approximately 85% of the neurons labeled were localized in the LGN (visual relay nucleus), while another 10% were localized in the LP (visual nonrelay). Less than 5% of the thalamic neurons projecting to V1 were in nonvisual relay nuclei. We found similar results when comparing the origin of TC neurons in the V1 of *Nrp2*$^{-/-}$ and *Nrp2* $^{+/-}$ mice using Fluorogold retrograde tracing (*Nrp2* WT mice, 5.3 ± 0.6 months; *Nrp2* KO mice, 5.3 ± 0.6 months; data not shown). Therefore, the abnormal TC connectivity observed at P7 (Demyanenko et al., 2011) has been repaired in adult *Nrp2*$^{-/-}$ mice and is absent in adult *PlxnA3*$^{-/-}$ mice.

Thalamocortical synaptic connectivity

We have shown so far that the supernumerary spines found in the sensory cortex were localized on L4 neurons and on the apical dendrites of L5 neurons, a segment of L5 neurons located in L4. To confirm that those supernumerary spines were functional, we performed *in vitro* whole-cell recordings in voltage clamp ($V_h = -70$ mV) and analyzed the miniature EPSCs (mEPSCs) in neurons located in V1 L4 and V1 L5 of *PlxnA3* KO and *PlxnA3* WT mice (Fig. 4*A*; *PlxnA3* WT mice, 4.9 ± 1.5 months; *PlxnA3* KO mice, 4.7 ± 1.5 months). The mEPSC frequency of L4 and L5 neurons was slightly, but significantly, higher in KO than in WT mice (Fig. 4*B*; L4 WT: 4.7 ± 5.8 Hz, n = 6815 intervals, 17 neurons; L4 KO: 5.2 ± 6.1 Hz, n = 4566 intervals, 5 neurons; Wilcoxon rank-sum test: $z_{value} = -5.00$, $p < 0.0001$; L5 WT: 4.1 ± 5.4 Hz, n = 7825 intervals, 13 neurons; L5 KO: 5.1 ± 7.7 Hz, n = 10,603 intervals, 13 neurons; Wilcoxon rank-sum test: $z_{value} = -13.98$, $p < 0.001$). The increase in miniature current frequency confirmed the results of previous studies showing that the supernumerary spines present on the neurons of the L4 and L5 of KO mice are functional (Tran et al., 2009; Demyanenko et al., 2014). The amplitude of L4 mEPSCs was similar for the WT and the mutant (L4 WT: 5.1 ± 3.8 pA, n = 6925 events, 17 neurons; L4 KO: 5.1 ± 2.4 pA, n = 4638 events, 5 neurons; Wilcoxon rank-sum test: $z_{value} = -0.20$, $p = 0.84$). In contrast, the amplitude of L5 mEPSCs was significantly larger in KO than in WT (Fig. 4*C*,*D*; L5 WT: 6.1 ± 4.9 pA, n = 7984 events, 13 neurons; L5 KO: 7.6 ± 7.4 pA, n = 10 806 events, 13 neurons; Wilcoxon rank-sum test: $z_{value} = -23.6$, $p < 0.0001$). This increase in amplitude could result from the perturbation of the homeostatic downscaling present in cortical neurons of mice lacking Nrp2 signaling (Wang et al., 2017).

To determine the impact of those functional supernumerary spines on the response of L4 and L5 neurons to thalamocortical inputs, we performed *in vitro* voltage-clamp recordings in V1 slices taken from *PlxnA3* KO or WT mice injected with a ChR2 AAV in the LGN. The LGN axon terminals located in V1 were activated with a blue light pulse (wavelength, 470 nm; duration, 2 ms; Fig. 5*A*). L4 was identified during the recordings by the abundance of thalamocortical axons (Fig. 5*B*, labeled in green). Neurons were patched both in L4 and L5. We then confirmed the glutamatergic nature of the evoked EPSCs by applying AMPA and NMDA receptor antagonists [Fig. 5*C*,*D*; L4: $amplitude_{Control}$ = 102 ± 39 pA (median ± median absolute deviation [m.a.d.]: $amplitude_{cnqx+AP\text{-}5}$ = 5 ± 7 pA; n = 8 neurons; Wilcoxon rank-sum test, $p = 0.0003$; L5: $amplitude_{Control}$ = 43 ± 47 pA; $amplitude_{CNQX+AP\text{-}5}$ = 3 ± 2 pA, n = 6 neurons; Wilcoxon rank-sum test, $p = 0.002$]. We then recorded the evoked currents induced by light pulses of incremental intensities (Fig. 5*E*, *F*). In L5 of *PlxnA3* KO mice, 46% of neurons (6 of 13) presented a dramatically increased sensitivity to the optogenetic stimulation of thalamocortical axons (Fig. 5*E*, response values outside the upper bound of the 95% confidence interval of the linear relationship between light stimulus intensity and response amplitude in L5 PlxnA3 WT) and were responding to a light intensity range similar to the one necessary to obtain responses in L4 neurons (Fig. 5*F*; 0.1–0.3 mW/mm^2). In L4, some *PlxnA3* KO neurons (2 of 5, 40%) also presented a response significantly greater than the response of L4 WT neurons (Fig. 5*F*, values outside of the 95% two-sided confidence interval of the WT population), suggesting that a subpopulation in L4 neurons could also be hyperexcitable.

As the supernumerary spine on L4 and L5 neurons are located within the L4 region, in an area dense in thalamocortical axons, we tested the hypothesis that the supernumerary spines found on those neurons could result from an excessive connectivity between the neurons of the visual thalamus (LGN) and the neurons of V1. To isolate monosynaptic responses coming from LGN axons from polysynaptic response arising from recurrent corticocortical connections, we measured the onset of the EPSC as well the timing of the different peaks of activity in response to the optogenetic activation of the LGN axons in L4 and L5 neurons (Fig. 6*A*). In WT, the EPSC onset in L5 WT neurons was

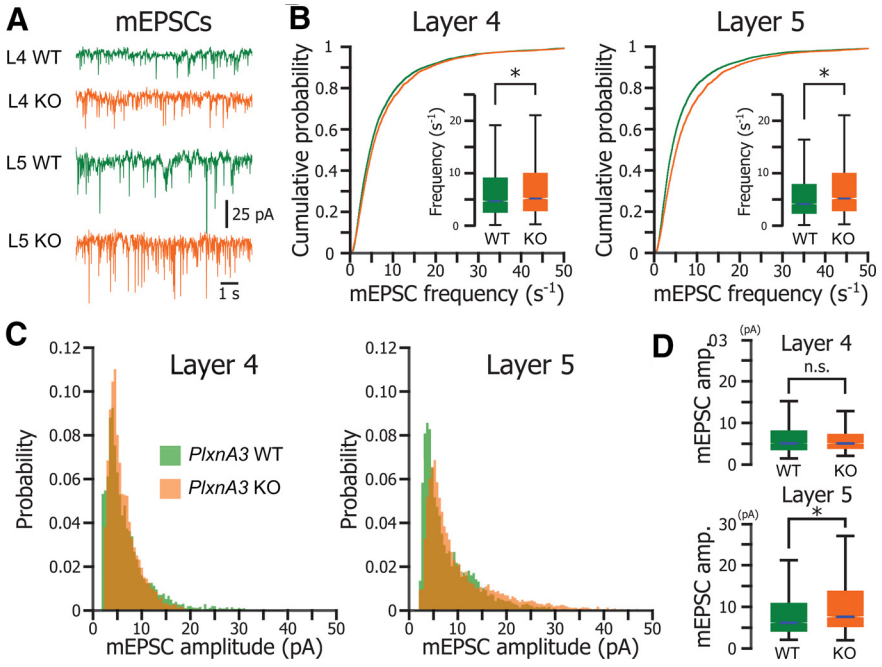

Figure 4. Miniature currents in the V1 of *PlxnA3* WT and *PlxnA3* KO mice. ***A***, Miniature EPSCs recorded in V1 L4 (top traces) and V1 L5 (bottom traces) of adult WT (green traces) and *PlxnA3* KO mice (orange traces). ***B***, Cumulative probability of the mEPSC frequency in *PlxnA3* WT and *PlxnA3* KO mice L4 (left) and L5 neurons (right). Inset, Box plot representation of the same data for statistical comparison. *$p < 0.0001$. ***C***, Probability distribution of the amplitude of mEPSCs in the L4 (left) and L5 (right) of WT (black) and *PlxnA3* KO mice. ***D***, Box plots summarizing the data shown in ***C*** and statistical comparison. *$p < 0.0001$.

significantly lagging compared with L4 WT neurons, as expected for a response composed to a major extent from polysynaptic inputs [Fig. 6*B*; L4 WT = 5.9 ± 1.3 ms, $n = 42$ trial sets in 19 neurons (12 mice); L5 WT = 9.0 ± 3.0 ms, $n = 43$ trial sets in 19 neurons (10 mice); Kruskal–Wallis test: χ^2 statistic = 23.8 $p = 1 \times 10^{-6}$]. The response initiation in L5 KO was also significantly delayed compared with L4 KO neurons [L4 KO = 5.6 ± 7.4 ms, $n = 24$ trial sets in 10 neurons (8 mice); L5 KO = 8.8 ± 46.5 ms, $n = 55$ trial sets in 20 neurons (7 mice); Kruskal–Wallis test: χ^2 statistic = 8.6, $p = 0.003$], but there was no difference between the response initiation timing of L5 WT and L5 KO neurons (Fig. 6*B*; Kruskal–Wallis test: χ^2 statistic = 0.03, $p = 0.87$), suggesting that L5 KO neurons were also receiving mostly polysynaptic inputs from thalamocortical neurons. Similarly, the response peaks occurred significantly later in L5 neurons than in L4 neurons for both WT and KO mice [Fig. 6*C*; L4 WT = 10.2 ± 6.3 ms, $n = 55$ peaks from 42 trial sets in 19 neurons (12 mice); L5 WT = 19.1 ± 9.2 ms, $n = 66$ peaks from 43 trial sets in 19 neurons (10 mice); Kruskal–Wallis test: χ^2 statistic = 26.2, $p = 3 \times 10^{-7}$; L4 KO = 11.3 ± 3.4 ms, $n = 27$ peaks from 24 trial sets in 10 neurons (8 mice); L5 KO = 19.4 ± 13.0 ms, $n = 59$ peaks from 55 trial sets in 20 neurons (7 mice); Kruskal–Wallis test: χ^2 statistic = 18.8, $p = 1 \times 10^{-5}$]. Finally, there was no significance difference in response peaks between the KO and WT (Fig. 6*D*; Kruskal–Wallis test: L4: χ^2 statistic = 0.03, $p = 0.86$; L5: χ^2 statistic = 0.11, $p = 0.75$). However, the response of the neurons from the L5 and L4 of KO mice that presented an hyperexcitability (Fig. 5*E*,*F*) started significantly earlier than the response of their WT counterparts [L5 WT = 9.0 ± 3.0 ms, $n = 43$ trial sets in 19 neurons (10 mice); L5 KO_{hyper} = 5.9 ± 5.2 ms, $n = 14$ trial sets in 6 neurons (four mice); χ^2 statistic = 9.44; $p = 0.002$; L4 WT = 5.9 ± 1.3 ms, $n = 42$ trial sets in 19 neurons (12 mice); L4 KO_{hyper} = 4.5 ± 0.9 ms, $n = 8$ trial sets in 3 neurons (2 mice); χ^2 statistic = 5.43; $p = 0.02$; Fig. 6*E*].

To determine whether the hyperexcitability and early response of L5 KO neurons was because of the presence of aberrant direct thalamocortical connections, we performed the optogenetic stimulation of thalamocortical axon in the presence of TTX and 4-AP (Fig. 6*F*). We first showed with L4 WT neurons that it was possible to obtain direct postsynaptic responses with TTX if 4-AP is added to the bath solution (Fig. 6*F*, left; Yamawaki et al., 2016). Then we tried to find direct connections between the thalamocortical axons and L5 neurons. Only a small fraction of L5 KO neurons (two of seven) and WT neurons (one of five) were directly innervated by thalamic afferents (Fig. 6*F*, middle). The percentages of responding L5 neurons in WT and KO were not significantly different, suggesting that the vast majority of supernumerary postsynaptic densities found on the apical dendrite of L5 KO neurons are not in contact with thalamocortical neurons (Fig. 6*G*; χ^2 test: χ^2 = 0.11, $p = 0.74$). Therefore, our experiments suggest that the hyperexcitability and early response of L5 KO neurons most likely results from aberrant corticocortical connections.

Functional connectivity in the cortex

To determine the effect of the supernumerary spines from L4 and L5 KO neurons on the functional connectivity of the cerebral cortex, we performed two-photon calcium imaging in the V1 of awake head-fixed mice placed on a spherical treadmill in front of a screen (Fig. 7*A*; *PlxnA3* WT mice, 4.7 ± 1.6 months; *PlxnA3* KO mice, 4.7 ± 1.4 months; *Nrp2* WT mice, 4.3 ± 1.5 months; *Nrp2* KO mice, 4.2 ± 1.3 months) displaying a series of six different orientation gratings drifting in either of the two directions (McClure and Polack, 2019). The calcium transients evoked in response to the visual stimuli were fed to a resampling-based Bayesian algorithm to determine the preferred orientation of the neurons (Fig. 7*A*; Cronin et al., 2010). We then computed the correlation between the activities of each neuronal pair recorded simultaneously (Fig. 7*B*) and ordered them as a function of the difference of preferred orientation between the two neurons. As expected, correlations were higher for neuronal pairs having similar preferred orientations (Δ preferred orientation, ~0) for all layers in both WT and KO mice (*Nrp2* WT and KO mice: Fig. 7*B–D*; *PlxnA3* WT and KO mice: Fig. 7*E–G*). When comparing *Nrp2* KO and *Nrp2* WT, the correlations of pairs having similar preferred orientations (pref. ± 30°), we found a larger correlation in L4 KO than in L4 WT [difference for pref. (median ± m.a.d), 24 ± 27%; effect size, medium; Cohen's $d = 0.45$; Fig. 7*B*], and in L5 KO compared with L5 WT (difference for pref., 46 ± 26%; effect size, large; Cohen's $d = 1.07$; Fig. 7*D*), but correlation was similar in L2/3 WT and KO (difference for pref., 5 ± 35%; effect size, no effect; Cohen's $d = -0.04$; Fig. 7*C*). This phenotype was also found when comparing correlation between neurons of similar preferred orientation in *PlxnA3* KO and

PlxnA3 WT. We did not find any difference in correlation between *PlxnA3* WT and KO in L2/3 (difference for pref., 1 ± 35%; effect size, no effect; Cohen's $d = 0.12$; Fig. 7*F*). However, the differences were smaller in L4 and L5 *PlxnA3* KO than the differences we had found between *Nrp2* KO and *Nrp2* WT (*PlxnA3* L4 difference for pref., 0 ± 25%; effect size, no effect; Cohen's $d = 0.14$; Fig. 7*E*; *PlxnA3* L5 difference for pref., 23 ± 23%; effect size, large; Cohen's $d = 0.83$; Fig. 7*G*). As Sema3F–Nrp2/PlxnA3 signaling could be involved in increasing the signal-to-noise ratio in L4 or L5 by removing connections between neurons of orthogonal (ortho.) or opposite (opp.) preferred orientation, we computed independently the difference of correlation for neuronal pairs of similar preferred orientation and same direction (pref. ± 30°), neuronal pairs of similar preferred orientation but opposite direction (opp.: pref., +180 ± 30°) and neuronal pairs of different preferred orientations (ortho.: pref., 90 ± 30°; Fig. 7*B–G*, insets). As the effect seemed stronger in L4 and L5 for orthogonal orientations, we performed a multivariate analysis of variance on the L4 and the L5 results using the tuning difference (pref., ortho, or opp.) and the genetic model *Nrp2* or *PlxnA3* as variable. We found a significant effect of tuning difference (L4: $F = 14.5$, $p = 0.0001$; L5: $F = 66.3$, $p < 0.001$) and the background (L4: $F = 3.6$, $p = 0.0275$; L5: $F = 13.78$, $p < 0.001$). These results suggest that the supernumerary spines found in L4 and L5 from the KO animals are connections between neurons having different preferred orientations that are normally pruned in WT during the cortical maturation.

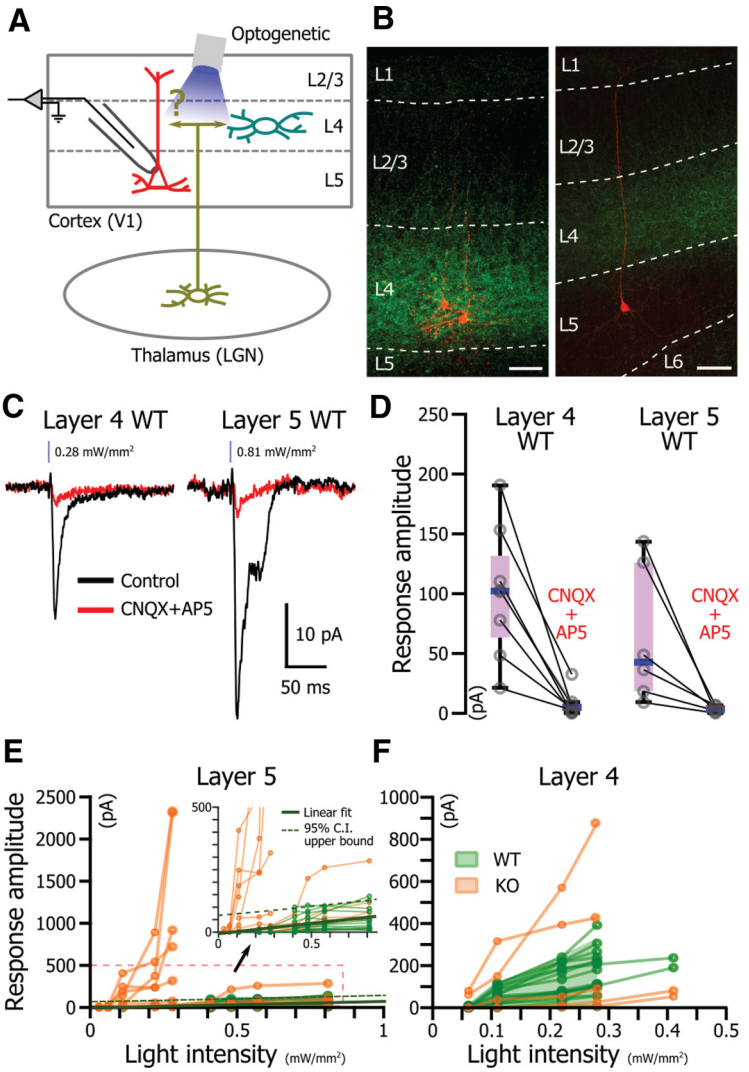

Figure 5. Response of V1 L4 and L5 neurons to the optogenetic stimulation of LGN thalamocortical axons in *PlxnA3* WT and *PlxnA3* KO mice. ***A***, Schematic representation of the experimental setup. ***B***, Confocal microscope images of two slices containing a total of three recorded neurons. Red channel, Recorded neurons filled with biocytin and reacted with streptavidin Alexa Fluor 594; green channel, axons expressing ChR2-YFP. ***C***, Mean response (average of 10 trials) of a L4 neuron (left) and a L5 neuron (right) of WT mice in response to the optogenetic stimulation of the thalamocortical axons (blue line) in the absence (control, black trace) and presence of glutamate antagonists (CNQX + AP-5). ***D***, Amplitude of the current evoked in L4 and L5 WT neurons by the optogenetic stimulation of thalamocortical axons in the absence (left) and the presence (right) of CNQX + AP-5. ***E***, Amplitude of the current response as a function of the stimulus intensity in L5 *PlxnA3* WT (Pinto et al., 2010) and L5 *PlxnA3* KO neurons (orange). Green solid line, Linear fit of the relationship between light intensity and response amplitude in L5 WT neurons; green dashed line, upper bound of the 95% confidence interval of the linear fit. Neurons with responses consistently above this line present a significant hyperexcitability compared with the L5 WT population. Inset, Enlargement on the evoked activity of L5 WT neurons. ***F***, Same representation as in ***E*** for neurons of L4. The green shaded area indicates the 95% confidence interval of the response of neurons recorded in the WT mouse population.

Discussion

The goal of this study was to understand the role of semaphorin–Nrp2/PlxnA3 signaling in the establishment of the adult functional connectivity of the cerebral cortex. Using a combination of neuroanatomy, electrophysiology, and functional imaging techniques, we (1) provided a detailed survey of the stereotypic dendritic spine defects found in the principal layers of sensory and motor cerebral cortices from *Nrp2* and *PlxnA3* knock-out mice, (2) uncovered that the inputs to the supernumerary spines found in L5 and L4 KO neurons are not from ectopic thalamocortical axons but could arise from corticocortical connections, and (3) determined the functional impact of those supernumerary spines on the primary visual cortical connectivity.

The first goal of this study was to clarify the location of the dendritic spine phenotype occurring in the absence of Nrp2 and PlxnA3. Indeed, each of the previous studies reporting defects in the absence of semaphorin–Nrp2/PlxnA3 signaling had only examined one or two particular layers in a single cortical area of some selected mutants. The first report of cortical synaptic transmission defects demonstrated the presence of supernumerary spines in the L5 of the somatosensory cortex of all three mouse mutants (*Sema3F*$^{-/-}$, *Nrp2*$^{-/-}$, and *PlxnA3*$^{-/-}$) and showed that this defect was not present in L2/3 (Tran et al., 2009). However, no measurement of the spine densities was performed in L4. In a later study, a lack of spine elimination was reported in V1 L4 neurons of *Sema3F* KO mice, but spine densities in V1 L5 and V1 L2/3 were not assessed. Thus, it remained unclear which layers were affected and whether the spine elimination controlled by Sema3F signaling was widespread or specific to particular cortical areas. Moreover, the presence of a posteroanterior gradient of Sema3F (Demyanenko et al., 2011) and the presence of aberrant projection of anterior thalamic nuclei neurons toward

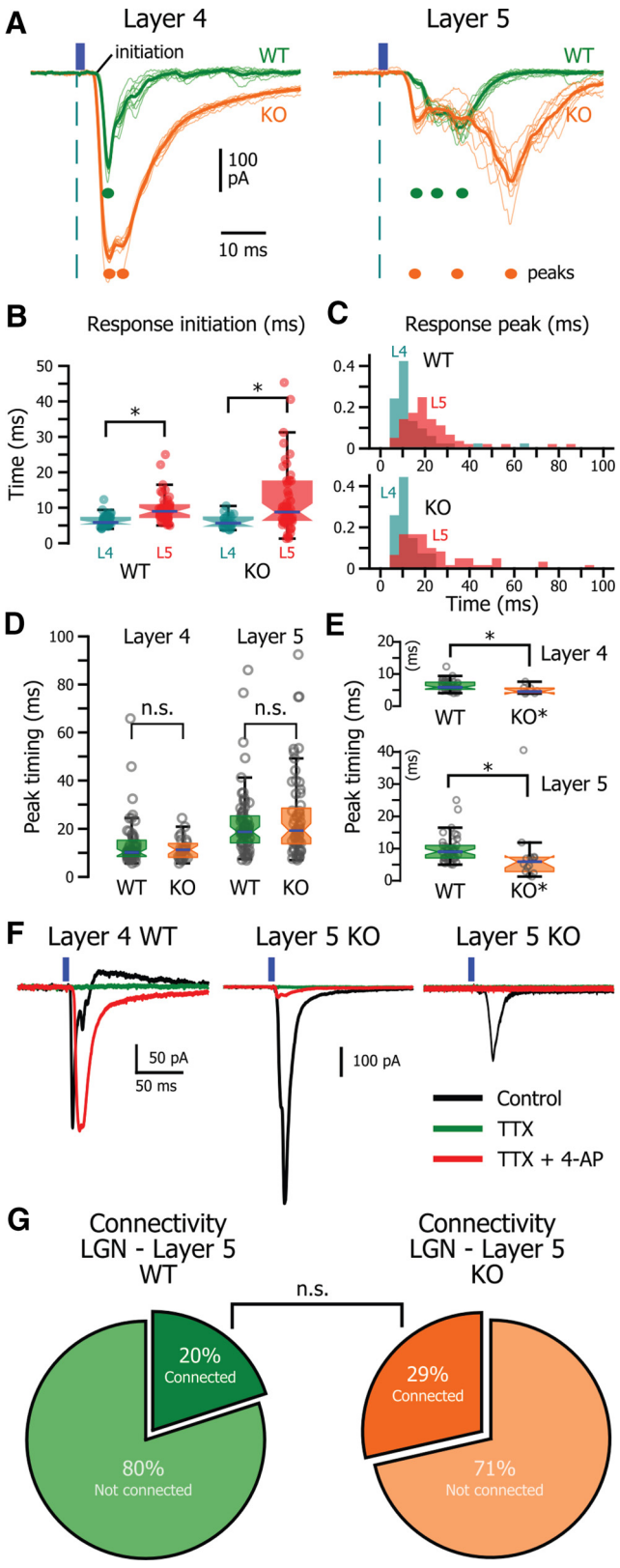

Figure 6. Direct thalamocortical connectivity to V1 L4 and V1 L5 neurons in *PlxnA3* WT and *PlxnA3* KO mice. ***A***, Left, Response of a WT (green trace) and a *PlxnA3* KO V1 L4 neuron (orange trace) to the optogenetic stimulation of the thalamocortical axons located in V1 (blue rectangle; intensity, 0.28 mW/mm^2). Thicker trace, Average of the 10 presented trials (light traces); dots, location of response peaks. Right, Same representation for WT and *PlxnA3* KO L5 neurons using 0.81 and 0.11 mW/mm^2 stimuli, respectively. ***B***, Timing of the optogenetic response initiation in the L4 and L5 WT and *PlxnA3* KO mice. *$p < 0.01$. ***C***, Distribution of the timings of the response peak in the L4 and L5 WT (top) and *PlxnA3* mice (bottom). ***D***, Timing of the peak of the current response in the L4 and L5 WT and *PlxnA3* KO mice. n.s., $p > 0.05$. ***E***, Response initiation for the WT and hyperexcitable KO neurons (KO*). *$p < 0.05$. ***F***, Left, Responses evoked in one L4 WT neuron by optogenetic stimulations of the thalamocortical axons in V1 in the absence (black traces, Control) or presence of TTX alone (green trace) or combined with 4-aminopyridine (red trace). Middle, L5 *PlxnA3* KO neurons showing direct connection to the LGN. Right, L5 *PlxnA3* KO neurons not connected to the LGN. ***G***, Proportion of L5 neurons in WT (left) and *PlxnA3* KO mice (right) showing direct thalamocortical connections. $\chi^2 = 0.11$, $p = 0.74$.

the posterior cortices found at P7 (Demyanenko et al., 2011) suggested that the pattern of aberrant spine numbers could follow an posteroanterior gradient in the adult. In this study, we have shown that in adult mice, similar stereotypical spine number defects can be found in L4 and L5 in all the analyzed cortices, with similar phenotypes from both *PlxnA3* and *Nrp2* KOs. Intriguingly, the supernumerary spine phenotype was stronger in *Nrp2* KO than in *PlxnA3* KO mice. While Nrp2 has been shown previously to preferentially bind with PlxnA3 to form a coreceptor for Sema3F (Yaron et al., 2005; Schwarz et al., 2008), we know that Nrp2 can also directly bind (or cross talk) with other type A plexin receptors (Yaron et al., 2005; Hernandez-Enriquez et al., 2015; Tan et al., 2019). In addition, Nrp2 may also be activated by other secreted semaphorins such as Sema3B, Sema3C, and Sema3G (Falk et al., 2005; Pascual et al., 2005; Sanyas et al., 2012; Tan et al., 2019). Therefore, the stronger phenotype seen in *Nrp2* knock-out animals could result from Nrp2 forming receptor complexes with other type A plexins or being activated by other secreted semaphorins in the cortex to mediate dendritic spine removal (Mohan et al., 2019).

The second goal of this study was to test the hypothesis that the supernumerary spines located on L5 and L4 neurons were of thalamic origin. Indeed, it had been shown in *PlxnA3* and *Nrp2* mice that the axons of the neurons of anterior thalamic nuclei projected toward posterior cortical areas at P7 (Demyanenko et al., 2011), and that V1 was therefore receiving direct connections from the ventrobasal thalamus and the ventrolateral thalamus, two thalamic nuclei connecting, respectively, with S1 and M1 in WT mice. Hence, we tested the hypothesis that those ectopic projections were still present in the adult mutants. We found that the primary visual cortices of both *PlxnA3* and *Nrp2* KO adult mice were displaying a normal pattern of connectivity with afferents coming from the LGN and LP. It has been shown previously that guidance defects occurring early in development can be repaired later. For example, a similar misguidance of nonvisual thalamocortical axons targeting V1 at P7 in the absence of Sema6A was also shown to be corrected in the adult (Little et al., 2009). However, this finding did not discard the hypothesis that the supernumerary spines found on the L5 and L4 neurons were originating from the LGN. Indeed, the supernumerary spines are found only on dendrites located where the density of thalamocortical axon is maximal (Fig. 5*B*). We therefore hypothesized that the role of semaphorin–Nrp2/PlxnA3 signaling was to prune direct connections between thalamocortical axons and L5 neurons and to remove the excess of thalamocortical connections on L4 neurons during the maturation of the cortical functional connectivity. However, our TTX experiments did not provide evidence of aberrant direct connections between thalamocortical and L5 neurons. Moreover, at the whole-population level, we did not find that L5 neurons responded to the optogenetic stimulation of the thalamocortical axons with the same timing as L4, which would be expected if L5 KO neurons were receiving direct thalamocortical connections.

While we could not find direct evidence that the spine pruned under the control of the semaphorin–Nrp2/PlxnA3 signaling are of thalamocortical origin, we found that the response of about half of L5 neurons recorded in *PlxnA3* KO mice presented with hyperexcitability in response to the stimulation of the thalamocortical axons. Our results also suggest that a fraction of L4 neurons could also be hyperexcitable. The timing of response initiation of the hyperexcitable L5 KO neurons in response to the stimulation of thalamocortical axons was significantly reduced compared with the response of L5 WT neurons, suggesting that the supernumerary spines belong to a connectivity pattern that short-circuit the normal path of visual information processing. As we did not find an aberrant direct connectivity between thalamocortical and L5 neurons, it is likely that the supernumerary connections found on the L5 apical dendrites originate from the recurrent corticocortical connections that normally amplify the thalamocortical signal (Morgenstern et al., 2016). The canonical circuit of sensory cortices implies that sensory information transits through L2/3 before reaching L5 (Douglas and Martin, 2004; but see Pluta et al., 2015). A short circuit between L4 and L5 would explain the low threshold and early response of L5 neurons following thalamocortical activation. Our experiments performed to compare the correlation between WT and KO provided additional information on the putative nature of the connections pruned under the control of Nrp2/PlxnA3 signaling. Cross-correlations can be used to estimate functional connectivity *in vivo* (Cohen and Kohn, 2011). We found that correlation between neuronal activities in L4 and L5 of *PlxnA3* and *Nrp2* KO mice was larger than in WT. This increase of correlation was not present in L2/3, suggesting that some maturation mechanisms compensated for the noisy L4 source. In line with the more severe dendritic spine phenotype found in *Nrp2* KO mice compared with *PlxnA3* KO mice, the correlation phenotype was stronger in *Nrp2* KO mice. Our results also indicate a higher correlation between L4 KO and L5 KO neurons when those neurons have dissimilar (orthogonal) preferred orientations (i.e., neurons unlikely to share bottom-up pathways). This suggests that Nrp2/Plxna3 signaling might be involved in the functional maturation of the cerebral cortex by removing connections between neurons belonging to different functional groups, improving the signal-to-noise ratio of the population activity. Finally, the global increase in correlated activity between neurons supports previous studies demonstrating that mice with defective Sema3F–Nrp2 signaling are prone to epilepsy (Sahay et al., 2005; Li et al., 2019; Eisenberg et al., 2021).

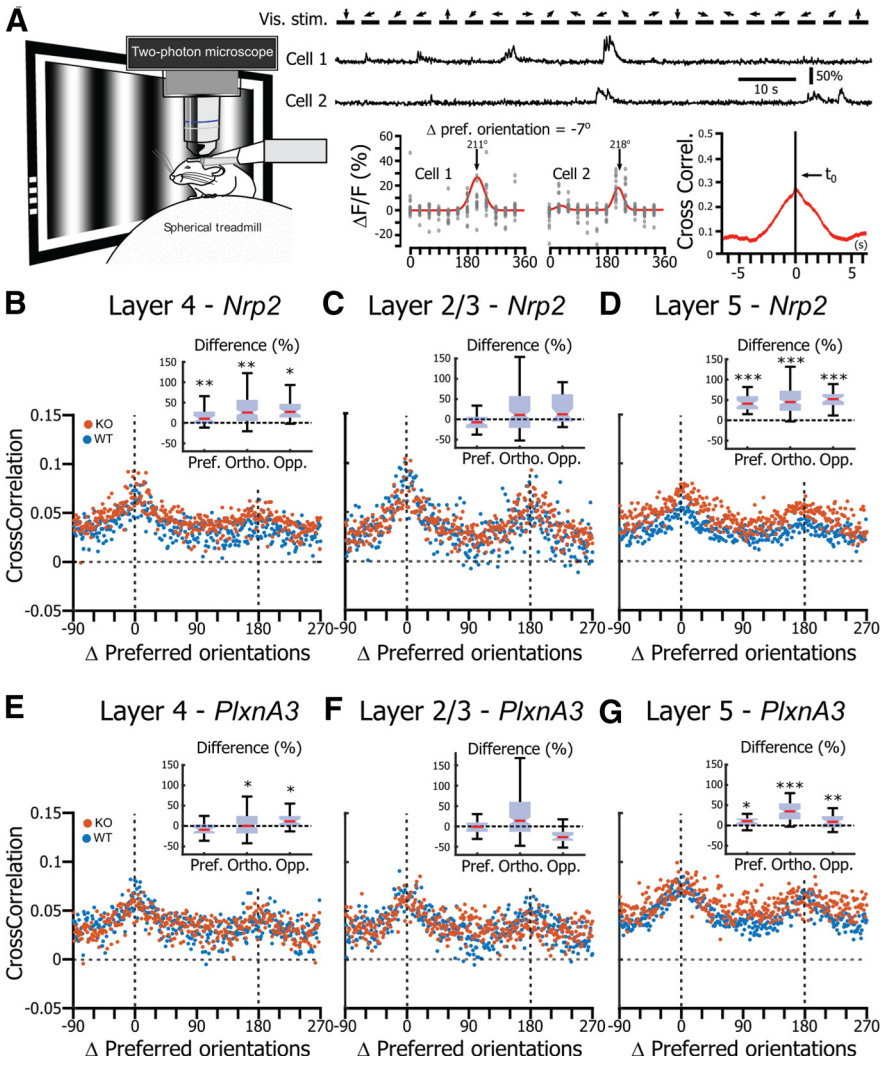

Figure 7. Neuronal activity correlation in V1 in the absence of Nrp2/PlxnA3 signaling. ***A***, Left, Schematic representation of the correlation analysis. Top, Example of two neurons recorded simultaneously while drifting gratings (arrows; 6 orientations, 2 directions) were presented on the screen. Bottom left, Orientation tuning curves of the two neurons shown above. Bottom right, Cross-correlogram of the neuronal activity of the two neurons recorded during the presentation of visual stimuli. ***B***, Correlation as a function of the distance (Δ) between the preferred orientations of the neuronal pairs for neurons recorded in L4 of *Nrp2* WT (blue) and *Nrp2* KO (orange) mice. Inset, Difference between the correlation measured in KO compared with WT when the neurons have similar pref. orientations, ortho. preferred orientations, or opp. preferred orientations. Asterisks indicate the effect size: *small effect size, **medium effect size, ***large effect size. ***C***, Same representation as in ***B*** for L2/3 *Nrp2* WT and *Nrp2* KO neurons. ***D***, Same representation as in ***B*** for L5 *Nrp2* WT and *Nrp2* KO neurons. ***E***, Same representation as in ***B*** for L4 *PlxnA3* WT and *PlxnA3* KO neurons. ***F***, Same representation as in ***C*** for L2/3 *PlxnA3* WT and *PlxnA3* KO neurons. ***G***, Same representation as in ***D*** for L5 *PlxnA3* WT and *PlxnA3* KO neurons.

Understanding the causal links existing between developmental signaling systems such as Sema3F–Nrp2/PlxnA3 and neuronal circuit functions is fundamental to better understanding of the etiology and semiology of several major neurologic disorders. Indeed, mutations of genes coding for axon guidance receptors or ligands are known to contribute to the etiology of several disorders, including Kallmann syndrome, epilepsies, and dyslexia (Van Battum et al., 2015). Mutations of Sema3F signaling are associated with autism spectrum disorders (ASDs; Pinto et al., 2010) and fragile X mental retardation (Menon and Mihailescu, 2007; Evans et al., 2012), disorders in which

neuronal morphology and structural connectivity were shown to be altered (Geschwind and Levitt, 2007; Amaral et al., 2008; McFadden and Minshew, 2013). Recent studies have also established a link between *Nrp2* gene polymorphisms and ASD predisposition (Wu et al., 2007; Hosseinpour et al., 2017), while polymorphisms of *NrCAM*, a modulator associated with the Sema3F signaling system, has been associated with ASD subpopulations having obsessive-compulsive behavior and mathematical ability (Docherty et al., 2010; Pinto et al., 2010). As the findings presented in this study suggest a key role of Nrp2/PlxnA3 signaling in the establishment of a functional recurrent corticocortical connectivity, further studies will be necessary to narrow down the identity of the spines eliminated under the control of the Sema3F–Nrp2/PlxnA3 signaling as well as the functional importance of such synaptic removal for sensory processing and sensory perception. Follow-up research could provide a structural support for recent hypotheses proposing that deficits in synapse elimination (Irwin et al., 2001) and abnormal connectivity within the cerebral cortex are responsible for ASD symptoms (Hutsler and Zhang, 2010).

References

Alvarez VA, Ridenour DA, Sabatini BL (2007) Distinct structural and ionotropic roles of NMDA receptors in controlling spine and synapse stability. J Neurosci 27:7365–7376.

Amaral DG, Schumann CM, Nordahl CW (2008) Neuroanatomy of autism. Trends Neurosci 31:137–145.

Bagri A, Cheng HJ, Yaron A, Pleasure SJ, Tessier-Lavigne M (2003) Stereotyped pruning of long hippocampal axon branches triggered by retraction inducers of the semaphorin family. Cell 113:285–299.

Brainard DH (1997) The Psychophysics Toolbox. Spat Vis 10:433–436.

Cohen MR, Kohn A (2011) Measuring and interpreting neuronal correlations. Nat Neurosci 14:811–819.

Cronin B, Stevenson IH, Sur M, Körding KP (2010) Hierarchical Bayesian modeling and Markov chain Monte Carlo sampling for tuning-curve analysis. J Neurophysiol 103:591–602.

Demyanenko GP, Riday TT, Tran TS, Dalal J, Darnell EP, Brennaman LH, Sakurai T, Grumet M, Philpot BD, Maness PF (2011) NrCAM deletion causes topographic mistargeting of thalamocortical axons to the visual cortex and disrupts visual acuity. J Neurosci 31:1545–1558.

Demyanenko GP, Mohan V, Zhang X, Brennaman LH, Dharbal KE, Tran TS, Manis PB, Maness PF (2014) Neural cell adhesion molecule NrCAM regulates semaphorin 3F-induced dendritic spine remodeling. J Neurosci 34:11274–11287.

Docherty SJ, Davis OS, Kovas Y, Meaburn EL, Dale PS, Petrill SA, Schalkwyk LC, Plomin R (2010) A genome-wide association study identifies multiple loci associated with mathematics ability and disability. Genes Brain Behav 9:234–247.

Douglas RJ, Martin KA (2004) Neuronal circuits of the neocortex. Annu Rev Neurosci 27:419–451.

Eisenberg C, Subramanian D, Afrasiabi M, Ziobro P, DeLucia J, Hirschberg PR, Shiflett MW, Santhakumar V, Tran TS (2021) Reduced hippocampal inhibition and enhanced autism-epilepsy comorbidity in mice lacking neuropilin 2. Transl Psychiat 11:537.

Evans TL, Blice-Baum AC, Mihailescu MR (2012) Analysis of the Fragile X mental retardation protein isoforms 1, 2 and 3 interactions with the G-quadruplex forming semaphorin 3F mRNA. Mol Biosyst 8:642–649.

Falk J, Julien F, Bechara A, Fiore R, Nawabi H, Zhou H, Hoyo-Becerra C, Bozon M, Rougon G, Grumet M, Püschel AW, Sanes JR, Castellani V (2005) Dual functional activity of semaphorin 3B is required for positioning the anterior commissure. Neuron 48:63–75.

Franklin KBJ, Paxinos G (2013) Paxinos and Franklin's the mouse brain in stereotaxic coordinates, Ed 4. Amsterdam: Academic.

Geschwind DH, Levitt P (2007) Autism spectrum disorders: developmental disconnection syndromes. Curr Opin Neurobiol 17:103–111.

Giger RJ, Cloutier JF, Sahay A, Prinjha RK, Levengood DV, Moore SE, Pickering S, Simmons D, Rastan S, Walsh FS, Kolodkin AL, Ginty DD, Geppert M (2000) Neuropilin-2 is required in vivo for selective axon guidance responses to secreted semaphorins. Neuron 25:29–41.

Hernandez-Enriquez B, Wu Z, Martinez E, Olsen O, Kaprielian Z, Maness PF, Yoshida Y, Tessier-Lavigne M, Tran TS (2015) Floor plate-derived neuropilin-2 functions as a secreted semaphorin sink to facilitate commissural axon midline crossing. Genes Dev 29:2617–2632.

Holtmaat A, Wilbrecht L, Knott GW, Welker E, Svoboda K (2006) Experience-dependent and cell-type-specific spine growth in the neocortex. Nature 441:979–983.

Hosseinpour M, Mashayekhi F, Bidabadi E, Salehi Z (2017) Neuropilin-2 rs849563 gene variations and susceptibility to autism in Iranian population: a case-control study. Metab Brain Dis 32:1471–1474.

Hota PK, Buck M (2012) Plexin structures are coming: opportunities for multilevel investigations of semaphorin guidance receptors, their cell signaling mechanisms, and functions. Cell Mol Life Sci 69:3765–3805.

Hoy JL, Niell CM (2015) Layer-specific refinement of visual cortex function after eye opening in the awake mouse. J Neurosci 35:3370–3383.

Hutsler JJ, Zhang H (2010) Increased dendritic spine densities on cortical projection neurons in autism spectrum disorders. Brain Res 1309:83–94.

Irwin SA, Patel B, Idupulapati M, Harris JB, Crisostomo RA, Larsen BP, Kooy F, Willems PJ, Cras P, Kozlowski PB, Swain RA, Weiler IJ, Greenough WT (2001) Abnormal dendritic spine characteristics in the temporal and visual cortices of patients with fragile-X syndrome: a quantitative examination. Am J Med Genet 98:161–167.

Kong Y, Janssen BJ, Malinauskas T, Vangoor VR, Coles CH, Kaufmann R, Ni T, Gilbert RJ, Padilla-Parra S, Pasterkamp RJ, Jones EY (2016) Structural basis for plexin activation and regulation. Neuron 91:548–560.

Li Z, Jagadapillai R, Gozal E, Barnes G (2019) Deletion of semaphorin 3F in interneurons is associated with decreased GABAergic neurons, autism-like behavior, and increased oxidative stress cascades. Mol Neurobiol 56:5520–5538.

Little GE, López-Bendito G, Rünker AE, García N, Piñon MC, Chédotal A, Molnár Z, Mitchell KJ (2009) Specificity and plasticity of thalamocortical connections in Sema6A mutant mice. PLoS Biol 7:e1000098.

McClure JP Jr, Polack PO (2019) Pure tones modulate the representation of orientation and direction in the primary visual cortex. J Neurophysiol 121:2202–2214.

McFadden K, Minshew NJ (2013) Evidence for dysregulation of axonal growth and guidance in the etiology of ASD. Front Hum Neurosci 7:671.

Menon L, Mihailescu MR (2007) Interactions of the G quartet forming semaphorin 3F RNA with the RGG box domain of the fragile X protein family. Nucleic Acids Res 35:5379–5392.

Mohan V, Wade SD, Sullivan CS, Kasten MR, Sweetman C, Stewart R, Truong Y, Schachner M, Manis PB, Maness PF (2019) Close homolog of L1 regulates dendritic spine density in the mouse cerebral cortex through semaphorin 3B. J Neurosci 39:6233–6250.

Morgenstern NA, Bourg J, Petreanu L (2016) Multilaminar networks of cortical neurons integrate common inputs from sensory thalamus. Nat Neurosci 19:1034–1040.

Pascual M, Pozas E, Soriano E (2005) Role of class 3 semaphorins in the development and maturation of the septohippocampal pathway. Hippocampus 15:184–202.

Pasterkamp RJ (2012) Getting neural circuits into shape with semaphorins. Nat Rev Neurosci 13:605–618.

Pinto D, et al. (2010) Functional impact of global rare copy number variation in autism spectrum disorders. Nature 466:368–372.

Pluta S, Naka A, Veit J, Telian G, Yao L, Hakim R, Taylor D, Adesnik H (2015) A direct translaminar inhibitory circuit tunes cortical output. Nat Neurosci 18:1631–1640.

Sahay A, Kim CH, Sepkuty JP, Cho E, Huganir RL, Ginty DD, Kolodkin AL (2005) Secreted semaphorins modulate synaptic transmission in the adult hippocampus. J Neurosci 25:3613–3620.

Sanyas I, Bozon M, Moret F, Castellani V (2012) Motoneuronal Sema3C is essential for setting stereotyped motor tract positioning in limb-derived chemotropic semaphorins. Development 139:3633–3643.

Schwarz Q, Waimey KE, Golding M, Takamatsu H, Kumanogoh A, Fujisawa H, Cheng HJ, Ruhrberg C (2008) Plexin A3 and plexin A4 convey semaphorin signals during facial nerve development. Dev Biol 324:1–9.

Shiflett MW, Martinez E, Khdour H, Tran TS (2017) Functions of neuropilins in wiring the nervous system and their role in neurological disorders. In: The neuropilins: role and function in health and disease (Neufeld G, Kessler O, eds), pp 125–149. Cham, Switzerland: Springer.

Stiles J, Jernigan TL (2010) The basics of brain development. Neuropsychol Rev 20:327–348.

Tan C, Lu NN, Wang CK, Chen DY, Sun NH, Lyu H, Körbelin J, Shi WX, Fukunaga K, Lu YM, Han F (2019) Endothelium-derived semaphorin 3G regulates hippocampal synaptic structure and plasticity via neuropilin-2/plexina4. Neuron 101:920–937.e13.

Tessier-Lavigne M, Goodman CS (1996) The molecular biology of axon guidance. Science 274:1123–1133.

Tran TS, Kolodkin AL, Bharadwaj R (2007) Semaphorin regulation of cellular morphology. Annu Rev Cell Dev Biol 23:263–292.

Tran TS, Rubio ME, Clem RL, Johnson D, Case L, Tessier-Lavigne M, Huganir RL, Ginty DD, Kolodkin AL (2009) Secreted semaphorins control spine distribution and morphogenesis in the postnatal CNS. Nature 462:1065–1069.

Van Battum EY, Brignani S, Pasterkamp RJ (2015) Axon guidance proteins in neurological disorders. Lancet Neurol 14:532–546.

Wang Q, Chiu SL, Koropouli E, Hong I, Mitchell S, Easwaran TP, Hamilton NR, Gustina AS, Zhu Q, Ginty DD, Huganir RL, Kolodkin AL (2017) Neuropilin-2/plexinA3 receptors associate with GluA1 and mediate Sema3F-dependent homeostatic scaling in cortical neurons. Neuron 96:1084–1098.e7.

Wu S, Yue W, Jia M, Ruan Y, Lu T, Gong X, Shuang M, Liu J, Yang X, Zhang D (2007) Association of the neuropilin-2 (NRP2) gene polymorphisms with autism in Chinese Han population. Am J Med Genet B Neuropsychiatr Genet 144B:492–495.

Yamawaki N, Suter BA, Wickersham IR, Shepherd GM (2016) Combining optogenetics and electrophysiology to analyze projection neuron circuits. Cold Spring Harb Protoc 2016:pdb.prot090084.

Yaron A, Huang PH, Cheng HJ, Tessier-Lavigne M (2005) Differential requirement for plexin-A3 and -A4 in mediating responses of sensory and sympathetic neurons to distinct class 3 semaphorins. Neuron 45:513–523.